Migration of Ga vacancies and interstitials in β-Ga$_2$O$_3$

Ymir K. Frodason,[1] Joel B. Varley [ORCID],[2] Klaus Magnus H. Johansen,[1] Lasse Vines,[1] and Chris G. Van de Walle [ORCID][3]

[1]*Department of Physics/Centre for Materials Science and Nanotechnology, University of Oslo, N-0318 Oslo, Norway*
[2]*Lawrence Livermore National Laboratory, Livermore, California 94550, USA*
[3]*Materials Department, University of California, Santa Barbara, California 93106-5050, USA*

Pathways and energy barriers for the migration of Ga vacancies (V_{Ga}) and Ga interstitials (Ga$_i$) in β-Ga$_2$O$_3$ are explored using hybrid functional calculations and the nudged elastic band method. Considering β-Ga$_2$O$_3$ as primarily being an n-type semiconductor, we focus on defect charge states relevant under such conditions: V_{Ga}^{3-}, Ga$_i^{3+}$, and Ga$_i^{+}$. Notably, we describe a mechanism by which V_{Ga} can transform between its different split configurations. In all cases, the intermediate state consists of a vacancy split between three Ga sites—a three-split vacancy—which enables passage over a significantly lower energy barrier. This is because it avoids the unfavorable simple vacancy at the tetrahedral Ga site. The proposed mechanism lowers the overall barrier for V_{Ga}^{3-} diffusion along the [001] crystal direction from 1.73 to 0.97 eV, whereas the 2.08 eV barrier for the [100] and [010] directions is unaffected. For Ga$_i^{3+}$, we obtain similar overall migration barriers of 0.72, 0.80, and 1.02 eV for the [010], [001], and [100] directions, respectively. Ga$_i^{+}$ exhibits a strong preference for diffusion within the large eight-sided channel; the overall migration barrier is 0.92 eV for the [010] direction, and 2.16 eV for the [001] and [100] directions. The limiting step for the two latter directions involves ionization of Ga$_i^{+}$ followed by a jump to an adjacent large eight-sided channel as Ga$_i^{3+}$. Our results are discussed in light of experimental observations of thermally activated recovery processes in irradiated material.

I. INTRODUCTION

Monoclinic gallium sesquioxide (β-Ga$_2$O$_3$) is attracting great interest as an oxide semiconductor, owing to its unique combination of an ultrawide band gap ($\sim$4.9 eV [1]), high and widely tunable n-type conductivity [2], and availability in the form of melt-grown single crystals and epitaxial layers [3,4]. This makes it a highly attractive material for high-performance power electronics.

Studying intrinsic defect migration in semiconductors is important both from a fundamental and technological viewpoint. Not only does it constitute a basic mechanism for matter transport, as in self-diffusion, but it also plays a key role in the processes induced by radiation damage. In addition, intrinsic defects serve as vehicles for the migration of impurities. A thorough grasp of intrinsic defect migration is thus foundational to understanding impurity diffusion, which is key for controlling dopant distributions in semiconductor devices. In particular, Ga vacancies (V_{Ga}) and interstitials (Ga$_i$) are likely to assist the migration of technologically important shallow donors substituting on the Ga site (e.g., Si$_{\text{Ga}}$ [5], Ge$_{\text{Ga}}$, Sn$_{\text{Ga}}$) and deep compensating acceptors (e.g., Fe$_{\text{Ga}}$, Mg$_{\text{Ga}}$ [6]), respectively [7,8]. Migration is also important for the electrical behavior of a defect, as it will determine whether a defect will be stable as an isolated defect, or diffuse and bind to other defects.

The low symmetry of the monoclinic crystal structure causes defects in β-Ga$_2$O$_3$ to come in many geometrical arrangements. For some defects, the various configurations can differ significantly in their electrical behaviors and be prominent under different conditions [9]. For example, in devices operating at high temperatures and electric fields, defect configurations can potentially be altered during operation and affect device stability [10,11]. Such observations make it important to study not just the barriers for long-range migration of defects, but also the transformation between different configurations. The low symmetry of β-Ga$_2$O$_3$ also results in anisotropic diffusion parameters, which must be considered when interpreting experimental results [10,12,13].

Previous theoretical reports on V_{Ga} and Ga$_i$ migration in β-Ga$_2$O$_3$ have employed semilocal exchange-correlation functionals [8,14] or focus on diffusion along only one crystal direction [15,16]. In the present work, we use hybrid functional calculations and the nudged elastic band (NEB) technique [17] to calculate migration barriers for V_{Ga} and Ga$_i$ in β-Ga$_2$O$_3$. We analyze the results to obtain the overall pathways and energy barriers for diffusion in the three different crystal directions. Notably, we identify a type of configuration for V_{Ga} which drastically lowers its energy barrier for migration. Finally, we discuss our results in the context of experimental observations in irradiated material.

II. METHODOLOGY

The first-principles calculations were performed within the framework of the generalized Kohn-Sham (KS) theory, using projector-augmented-wave pseudopotentials [18,19], as implemented in VASP [20]. The semicore Ga 3d electrons were

treated explicitly as valence electrons. For structural optimization of β-Ga$_2$O$_3$ and calculation of defect formation energies, we used the screened hybrid exchange-correlation functional of Heyd, Scuzeria, and Ernzerhof (HSE) [21,22]. The fraction of Hartree-Fock exchange was adjusted to $\alpha = 0.33$, while the screening parameter was kept at $\mu = 0.2$ Å [23]. This parametrization reproduces the experimental direct band gap value of 4.9 eV [1] and provides lattice parameters ($a = 12.23$ Å, $b = 3.03$ Å, $c = 5.79$ Å, and $\beta = 103.8$) in close agreement with experimental data [24].

Most defects were simulated in a 160-atom supercell ($1 \times 4 \times 2$ repetition of the conventional unit cell). Due to the more extended nature of three-split Ga vacancy configurations (defined in Sec. III A 1), a larger 240-atom supercell ($1 \times 4 \times 3$ repetition) was required to obtain converged results for these configurations. An energy cutoff of 400 eV was used for the plane-wave basis set, and a single special k point at (0.25,0.25,0.25) was employed for integrations over the Brillouin zone [25].

Formation energies and thermodynamic charge-state transition levels were calculated as described in Ref. [26]. For example, the formation energy of V_{Ga}^q is given by

$$E^{\text{f}}\left(V_{\text{Ga}}^q\right) = E_{\text{tot}}\left(V_{\text{Ga}}^q\right) - E_{\text{tot}}(\text{Ga}_2\text{O}_3) + \mu_{\text{Ga}} + qE_{\text{F}} + \Delta^q, \tag{1}$$

where $E_{\text{tot}}[V_{\text{Ga}}^q]$ and $E_{\text{tot}}[\text{Ga}_2\text{O}_3]$ are the total energies of the supercell holding V_{Ga} in charge state q and the pristine crystal, respectively. The removed Ga atom is placed in a reservoir with chemical potential μ_{Ga}, and electrons are exchanged with the Fermi level E_{F}, which is conventionally referenced to the valence-band maximum. The Ga chemical potential is subject to upper and lower bounds: For the upper (Ga-rich limit), μ_{Ga} is given by the calculated energy per atom in pure Ga (μ_{Ga}^0). For the lower (O-rich limit), μ_{O} is determined by the energy of O in an O$_2$ molecule (μ_{O}^0), and μ_{Ga} is given by the thermodynamic stability condition of β-Ga$_2$O$_3$, i.e., $\mu_{\text{Ga}} = \mu_{\text{Ga}}^0 + \frac{1}{2}\Delta H_f(\beta\text{-Ga}_2\text{O}_3)$, where $\Delta H_f(\beta\text{-Ga}_2\text{O}_3) = -10.22$ eV is the calculated heat of formation of β-Ga$_2$O$_3$. Finally, the term Δ^q is a finite-size correction for charged defects, calculated here by following the procedure outlined in Refs. [27,28].

Migration barriers were calculated using the climbing-image NEB method [17], converging the forces to within 30 meV/Å. Due to the high computational cost of NEB calculations with a hybrid functional, initial calculations were performed using the strongly constrained and appropriately normed (SCAN) [29] semilocal functional, keeping the lattice parameters fixed to those computed using HSE. These NEB calculations were performed using 5–11 images between the initial and final structures. Next, NEB calculations at the HSE level were performed starting from the geometries obtained from the SCAN NEB calculations [30], and allowing additional relaxation at the HSE level. For V_{Ga}^{3-} and Ga$_i^{3+}$, we found it sufficient to perform one-shot HSE calculations (no additional relaxation), and full NEB calculations were performed only for the barriers limiting diffusion in the three crystal directions. The mean average difference between the resulting SCAN and HSE migration barriers is about 0.1 eV. In the following, we present only HSE results. The reported migration barriers do not include finite-size corrections
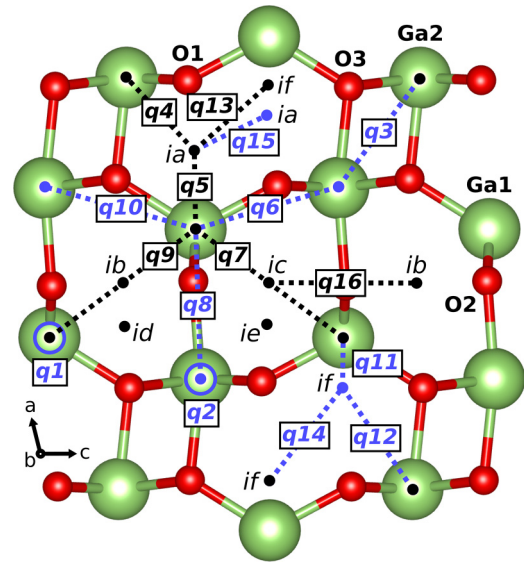

FIG. 1. Ball-and-stick model [33] of the monoclinic β-Ga$_2$O$_3$ structure with a schematic representation of 16 different migration paths ($q1$–$q16$) between Ga and interstitial sites [14]. The Ga, O, and interstitial sites (*ia*, *ib*, *ic*, *id*, *ie*, and *if* [32]) are labeled. Migration paths $q1$ and $q2$ (circles) are along the [010] direction. The paths shown in blue have components along [010], while the black ones do not

because we find its magnitude to be similar for the initial, final and transition-state images [14].

III. RESULTS AND DISCUSSION

Figure 1 shows the crystal structure of β-Ga$_2$O$_3$ with Ga sites (Ga1 and Ga2), O sites (O1, O2, and O3) and interstitial sites (*ia*, *ib*, *ic*, *id*, *ie*, and *if*) labeled in accordance with previous works [9,14,31,32]. Also included are 16 migration paths between Ga and interstitial sites. For these paths, we have adopted the $q1$–$q10$ notation introduced in Ref. [14], but have included six additional paths, $q11$–$q16$, relevant for Ga$_i$ migration. There are four channels along the [010] direction: a large eight-sided channel (with *ia* and *if* sites), two irregular-hexagon shaped ones (one with *ib* and *id*, and one with *ic* and *ie* sites), and a small rhombic one [14].

A. Defect formation energies and configurations

Before addressing migration, we revisit the structural and electronic properties of V_{Ga} and Ga$_i$. Figure 2 shows the relaxed structures of different configurations of V_{Ga} and Ga$_i$, and Fig. 3 shows their formation energies.

1. Ga vacancy

Previous theoretical studies have revealed five different configurations for V_{Ga} in β-Ga$_2$O$_3$ [14,31]: In addition to V_{Ga1} and V_{Ga2}, there are three energetically favorable split-vacancy configurations in which V_{Ga} is shared between *two* Ga sites with one Ga$_i$ residing between them, as shown in Figs. 2(a)–2(c). The three different split-vacancy configurations include $V_{\text{Ga2}}\text{Ga}_{ia}V_{\text{Ga1}}$ ($q4q5$), $V_{\text{Ga1}}\text{Ga}_{ib}V_{\text{Ga1}}$ ($q9q9$), and $V_{\text{Ga1}}\text{Ga}_{ic}V_{\text{Ga1}}$ ($q7q7$), where the paths connecting the
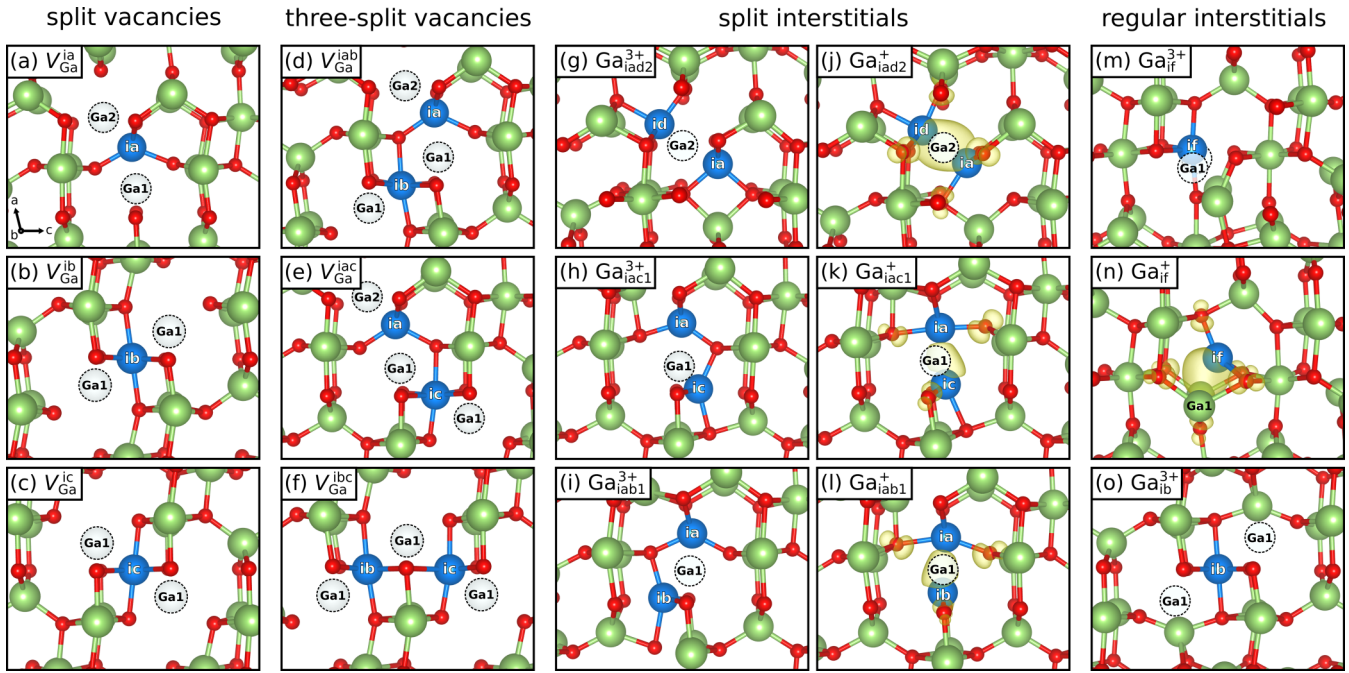
FIG. 2. Relaxed defect structures viewed along the b axis for (a)–(c) split Ga vacancies (V_{Ga}^{ia}, V_{Ga}^{ib}, V_{Ga}^{ic}), (d)–(f) three-split Ga vacancies (V_{Ga}^{iab}, V_{Ga}^{iab}, V_{Ga}^{ibc}), (g)–(l) split Ga interstitials (Ga$_{iac1}$, Ga$_{iab1}$, Ga$_{iad2}$), and (m)–(o) regular Ga interstitials (Ga$_{ib}$, Ga$_{if}$). Interstitial Ga ions and vacant Ga sites are highlighted by the blue spheres and translucent dotted circles, respectively. For Ga$_i^+$, the electron density of the deep donor state is represented by a yellow isosurface set to 10% of the maximum.

interstitial and two vacancies are given in parentheses; these configurations are labeled using a shorthand notation as V_{Ga}^{ia}, V_{Ga}^{ib}, and V_{Ga}^{ic}, respectively [14,31,34]. We note that there is also experimental evidence for the formation of split vacancy

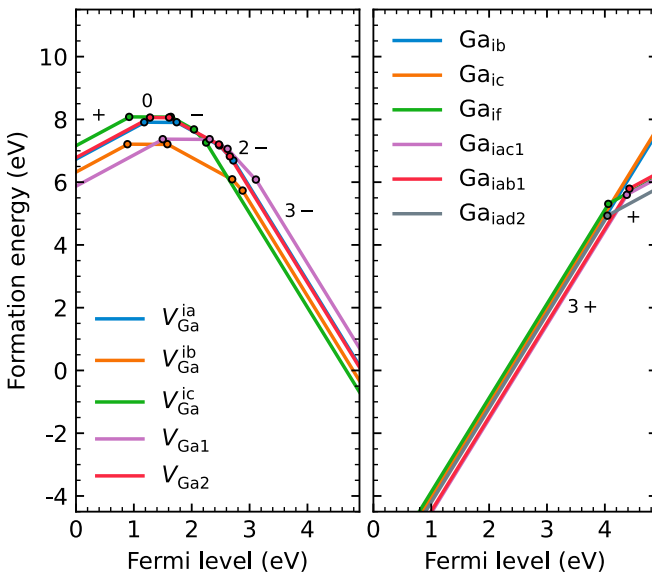FIG. 3. Calculated formation energies of V_{Ga} and Ga$_i$ in different configurations as a function of Fermi-level position from the valence-band maximum to the conduction-band minimum under intermediate conditions (halfway between the Ga-rich and O-rich limits). Formation energies under other conditions can be obtained by referring back to equations such as Eq. (1).

configurations of V_{Ga} in β-Ga$_2$O$_3$, e.g., from infrared spectroscopy [35,36], electron spin resonance [37,38], scanning transmission electron microscopy [32], and positron annihilation spectroscopy [39] data.

Recently, Fowler *et al.* [40] suggested that that a concerted movement of two Ga atoms could be more favorable than passing through V_{Ga1} when transforming between V_{Ga}^{ib} and V_{Ga}^{ic} configurations. Investigating this possibility, we have identified three additional favorable configurations of V_{Ga}, which, as detailed in Sec. III B 1, prove to be crucial for its migration. All three configurations consist of a V_{Ga} shared between *three* Ga sites, connected by two Ga$_i$, which we refer to as three-split vacancies. The three structures are shown in Figs. 2(d)–2(f), and are labeled as V_{Ga}^{iab}, V_{Ga}^{iac}, and V_{Ga}^{ibc} using a similar shorthand notation. In terms of their path connections, the three-split vacancies can be denoted as ($q4q5q9q9$) for V_{Ga}^{iab}, ($q4q5q7q7$) for V_{Ga}^{iac}, and ($q7q7q9q9$) for V_{Ga}^{ibc}.

V_{Ga} behaves as a deep triple acceptor, and can bind up to four holes, resulting in charge states ranging from 1+ to 3− in the band gap [15,41]. In line with magnetic resonance data [42], each hole is spatially localized at a single nearest-neighbor O ion in the form of a small polaron [43] (in some cases two O ions share the hole [44]). For each charge state, several different O sites are in principle available for localization of the hole(s), and the energy differences can be significant [44]. The formation energies shown in Fig. 3 correspond to the lowest-energy hole configuration for each charge state of V_{Ga}.

Although V_{Ga} can occur in different charge states, β-Ga$_2$O$_3$ is usually n type, and hence we consider the 3− charge state to be most relevant for the calculation of migration

barriers. Moreover, the 1+ to 2− charge states have relatively high formation energies and are therefore unlikely to form under equilibrium conditions.

2. Ga interstitial

The Ga interstitial is predicted to behave as a deep triple donor with a negative-U $(3 + /+)$ level near the conduction-band minimum (CBM), as shown in Fig. 3. In agreement with recent HSE calculations [7], we find that Ga_i prefers to form split-interstitial configurations in which two Ga ions share a Ga site, as shown in Figs. 2(g)–2(l). Regular interstitial configurations with Ga residing on the tetrahedral *ia*, *id*, and *ie* sites are found to be unstable, whereas those having Ga on the octahedral *ib*, *ic* [41], and *if* [45] sites are metastable. Only the Ga_{ib} and Ga_{if} regular interstitial configurations are shown in Figs. 2(m)–2(o), as Ga_{ic} is structurally similar to Ga_{ib}. In the 3+ charge state, the three metastable regular interstitial configurations lead to strong symmetrical displacements of the two adjacent Ga1 ions out of their sites, and could thus be viewed as three Ga ions sharing two Ga1 sites. However, the interstitial can easily relax towards one of the Ga1 sites, resulting in a split-interstitial configuration with two Ga ions sharing one site. The energetically preferred split-interstitial configuration differs for the two stable charge states of Ga_i. For 3+, the Ga1 site is preferred, and the two Ga atoms comprising the split interstitial are displaced towards the *ia* and *ic* sites, here denoted as Ga_{iac1}. For 1+, the Ga2 site is preferred, and the Ga ions are displaced towards the *ia* and *id* sites (Ga_{iad2}). Note that, for most Ga_i configurations, the local lattice relaxation is strong and the interstitial Ga ions are located somewhat off the ideal *ia*–*if* positions, but the configurations are still labeled using these sites.

For the Ga_i configurations displaying a $(3 + /+)$ level in Fig. 3, the 1+ charge state corresponds to a fully occupied KS defect state located deep within the band gap. The yellow isosurfaces in Fig. 2 show the corresponding electron density. For split configurations, the electrons are shared mainly between the two Ga ions comprising the split interstitial, which form a Ga-Ga dimer bond [9,46]. For the regular interstitials, the deep state is only stabilized for Ga_{if}. As shown in Fig. 2, Ga_{if}^{+} is located slightly off the octahedral *if* site and has threefold coordination, and a Ga-Ga dimer is formed with each of the two adjacent Ga1 ions. The local lattice relaxation is also minor compared to other configurations [45].

Previous HSE calculations have shown that similar Ga-Ga dimer states are formed by the $V_{Ga}V_O$ divacancy [9] and the Ga_O antisite [15] in β-Ga_2O_3, which are associated with negative-U $(−/3−)$ and $(3 + /+)$ levels, respectively, located in the band gap near the CBM. For $V_{Ga}V_O$, the strength of the Ga-Ga dimers was found to correlate with the coordination environments of the two Ga ions, where lower coordination numbers led to $(−/3−)$ levels at lower Fermi-level positions [9]. A similar trend between the $(3 + /+)$ level positions and coordination environments of the Ga ions is found here for Ga_i, e.g., no Ga-Ga dimer is stabilized for Ga_{ib} and Ga_{ic} in which the interstitial Ga ions have sixfold coordination.

As previously noted by Zacherle *et al.* [45] and Kyrtsos *et al.* [14], the PBE functional fails to stabilize the deep 1+ charge state of Ga_i. This is due to the severe band-gap

TABLE I. Migration barriers (E_m) for $V_{Ga}^{3−}$, Ga_i^{3+} and Ga_i^{+} along the paths $q1$–$q16$, as obtained from HSE calculations. The arrows indicate the direction of the transformation. For Ga_i, certain transformations consists of multiple paths because the Ga_{ia} configuration between the paths is unstable.

Transformation	Path	E_m (eV) $\rightarrow$	$\leftarrow$
$V_{Ga1} \rightleftharpoons V_{Ga1}$	$q1$	1.09	1.09
$V_{Ga2} \rightleftharpoons V_{Ga2}$	$q2$	1.29	1.29
$V_{Ga2} \rightleftharpoons V_{Ga2}$	$q3$	2.67	2.67
$V_{Ga2} \rightleftharpoons V_{Ga}^{ia}$	$q4$	0.66	0.53
$V_{Ga}^{ia} \rightleftharpoons V_{Ga1}$	$q5$	0.87	0.42
$V_{Ga2} \rightleftharpoons V_{Ga1}$	$q6$	1.36	0.78
$V_{Ga}^{ic} \rightleftharpoons V_{Ga1}$	$q7$	1.64	0.34
$V_{Ga2} \rightleftharpoons V_{Ga1}$	$q8$	2.19	1.61
$V_{Ga}^{ib} \rightleftharpoons V_{Ga1}$	$q9$	1.22	0.43
$V_{Ga2} \rightleftharpoons V_{Ga1}$	$q10$	2.16	1.58
$V_{Ga}^{ic} \rightleftharpoons V_{Ga}^{ibc}$	$q9$	0.97	0.69
$V_{Ga}^{ibc} \rightleftharpoons V_{Ga}^{ib}$	$q7$	0.61	0.46
$V_{Ga}^{ic} \rightleftharpoons V_{Ga}^{iac}$	$q4$	0.81	0.35
$V_{Ga}^{iac} \rightleftharpoons V_{Ga}^{ia}$	$q7$	1.05	0.66
$V_{Ga}^{ib} \rightleftharpoons V_{Ga}^{iab}$	$q4$	0.52	0.63
$V_{Ga}^{iab} \rightleftharpoons V_{Ga}^{ia}$	$q9$	0.92	0.40
$Ga_{iac1}^{3+} \rightleftharpoons Ga_{iad2}^{3+}$	$q5q4$	0.28	0.09
$Ga_{iac1}^{3+} \rightleftharpoons Ga_{ic}^{3+}$	$q7$	0.74	0.14
$Ga_{iab1}^{3+} \rightleftharpoons Ga_{ib}^{3+}$	$q9$	0.55	0.23
$Ga_{iac1}^{3+} \rightleftharpoons Ga_{if}^{3+}$	$q11$	0.72	0.01
$Ga_{iad2}^{3+} \rightleftharpoons Ga_{if}^{3+}$	$q12$	0.55	0.04
$Ga_{iac1}^{3+} \rightleftharpoons Ga_{if}^{3+}$	$q5q13$	1.02	0.31
$Ga_{iad2}^{3+} \rightleftharpoons Ga_{if}^{3+}$	$q4q13$	1.15	0.64
$Ga_{iac1}^{3+} \rightleftharpoons Ga_{iac1}^{3+}$	$q5q15q5$	1.44	1.44
$Ga_{iac1}^{3+} \rightleftharpoons Ga_{iab1}^{3+}$	$q16$	0.63	0.38
$Ga_{iad2}^{+} \rightleftharpoons Ga_{iac1}^{+}$	$q4q5$	0.92	0.56
$Ga_{if}^{+} \rightleftharpoons Ga_{iac1}^{+}$	$q11$	0.52	0.52
$Ga_{iad2}^{+} \rightleftharpoons Ga_{if}^{+}$	$q12$	1.14	0.78
$Ga_{if}^{+} \rightleftharpoons Ga_{iac1}^{+}$	$q13q5$	0.52	0.52
$Ga_{iad2}^{+} \rightleftharpoons Ga_{if}^{+}$	$q4q13$	1.10	0.74
$Ga_{if}^{+} \rightleftharpoons Ga_{if}^{+}$	$q14$	0.90	0.90
$Ga_{iac1}^{+} \rightleftharpoons Ga_{iab1}^{+}$	$q16$	0.15	0.01

underestimation, which causes the aforementioned KS defect state to be resonant with the conduction band. Interestingly, we find that the SCAN functional is capable of describing the Ga-Ga dimer formation for the Ga interstitial, which has enabled us to perform initial NEB calculations at the semilocal level also for Ga_i^{+}. Under *n*-type conditions, 1+ is the stable charge state for Ga_i. However, since Ga_i^{+} can be readily ionized [47], migration of Ga_i^{3+} is considered especially important.

B. Migration pathways and energy barriers

Calculated migration barriers for V_{Ga} and Ga_i for all individual $q1$–$q16$ paths are listed in Table I. Based on these barriers, we have worked out the overall diffusion path and migration barrier that must be surmounted in order for the lowest energy structure to move into an equivalent adjacent site in the three different crystal directions. The overall migration
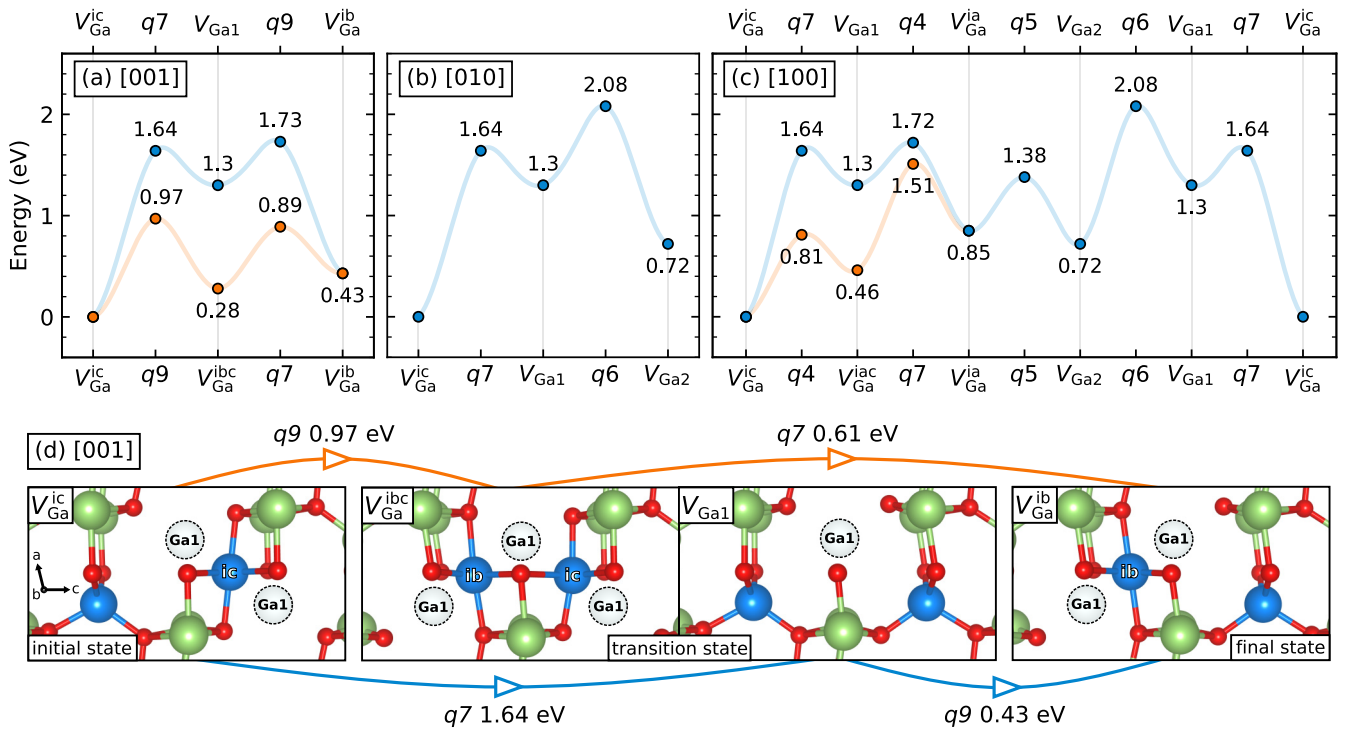
FIG. 4. Overall barriers and paths for $(V_{Ga}^{ic})^{3-}$ migration along the (a) [001], (b) [010], and (c) [100] crystal directions. For the [001] and [010] directions, only the first half of the path is shown, as the second half is equivalent to the first by symmetry. Orange lines show the lower-energy paths emerging when three-split vacancies are considered. (d) Structures showing the initial (V_{Ga}^{ic}), final (V_{Ga}^{ib}) and two different intermediate states (V_{Ga1} or V_{Ga}^{ibc}) for migration along the [001] direction.

pathways are obtained by connecting individual $q1$–$q16$ paths between different configurations, and can thus be understood by referring to Figs. 1 and 2. The pathways are also described in the text. As an additional aid, videos created from the NEB images resulting from the initial SCAN calculations can be found in the Supplemental Material [48].

1. Ga vacancy

For V_{Ga}, we consider only the $3-$ charge state, in which V_{Ga}^{ic} is the preferred configuration. Figure 4 shows the overall migration paths and barriers for each crystal direction. We restrict our initial analysis to include only the five configurations V_{Ga1}, V_{Ga2}, V_{Ga}^{ia}, V_{Ga}^{ib}, V_{Ga}^{ic} (only the blue lines in Fig. 4), that is, excluding the three-split vacancies. Starting from V_{Ga}^{ic}, the only available jump is then $q7$, which results in the highest-energy configuration V_{Ga1}. From here, migration along [001] shows the lowest overall barrier of 1.73 eV, and proceeds through the route $q7 \rightarrow q9 \rightarrow q9 \rightarrow q7$. In Fig. 4(a), this is shown only for the first half of the path, as the second half is equivalent to the first by symmetry. The vacancy migrates by alternating between V_{Ga}^{ic} and V_{Ga}^{ib} via the V_{Ga1} configuration. For migration along the two remaining directions, [010] and [100], the overall barrier is 2.08 eV in both cases. As shown in Fig. 4(b) and 4(c), the respective diffusion paths are $q7 \rightarrow q6 \rightarrow q6 \rightarrow q7$ and $q7 \rightarrow q4 \rightarrow q5 \rightarrow q6 \rightarrow q7$, and the barriers are equal because the limiting jump is $q6$ in both cases. Migration along [010] proceeds through consecutive $q6$ jumps, alternating between V_{Ga1} and V_{Ga2}. Alternate paths along [010], such as $q1$ migration directly along the b axis from V_{Ga1} to V_{Ga1}, are only

~ 0.2 eV higher. For [100], V_{Ga1} crosses the large eight-sided channel via the V_{Ga}^{ia} configuration through jumps $q4$ and $q5$, resulting in V_{Ga2}. The subsequent $q6$ jump from V_{Ga2} to V_{Ga1} is required in order to finally reach the next equivalent V_{Ga}^{ic} along the [100] direction through a $q7$ jump. Note that only the $q4$, $q5$, $q6$, $q7$, and $q9$ jumps are required for V_{Ga} diffusion, where all but $q6$ involve the ia, ib, or ic sites.

We now include the three-split vacancy configurations in our analysis of the V_{Ga} migration paths. As shown by the orange lines in Fig. 4(a) and 4(c), these configurations enable substantially lower migration barriers. Specifically, the barriers to transform between different split vacancy configurations are lowered. This is because the three-split configurations provide an intermediate state that avoids the unfavorable V_{Ga1} configuration that is 1.3 eV above V_{Ga}^{ic} in energy [40]. The corresponding energy differences for the V_{Ga}^{iab}, V_{Ga}^{iac}, and V_{Ga}^{ibc} configurations are only 0.37, 0.46, and 0.17 eV, respectively. Comparing the two mechanisms in terms of the $q1$–$q10$ jumps, their order is simply reversed. For example, V_{Ga}^{ic} transforms into V_{Ga}^{ib} via the path $q9 \rightarrow q7$ rather than $q7 \rightarrow q9$, as illustrated in Fig. 4(d). In terms of diffusion, the proposed mechanism affects the overall barrier only for the [001] direction, where the migration proceeds by alternating between V_{Ga}^{ic} and V_{Ga}^{ib}. Migration in the other directions is still limited by the $q6$ jump, which is not a transformation between split-vacancy configurations. With the three-split vacancy mechanism, the overall migration barrier along [001] is only 0.97 eV, i.e., the previous 1.73 eV barrier is almost halved. For migration along the two remaining directions, the overall barrier remains 2.08 eV.
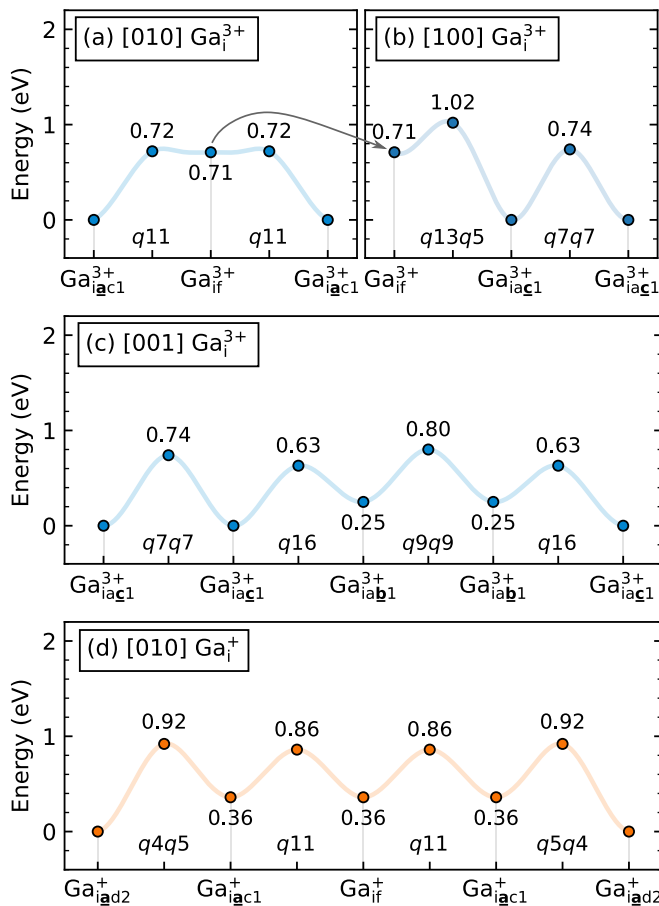
FIG. 5. Overall barriers and paths for Ga_i^{3+} migration (blue) along (a) [010], (b) [100], and (c) [001], and for Ga_i^+ migration (orange) along (d) [010]. In (b), the first step is omitted because it is equivalent to the first step shown in (a), as indicated by the arrow. As described in the text, Ga_i^+ migration along the [100] and [001] directions (not shown) is limited by thermal ionization of Ga_{iac1}^+ into Ga_{iac1}^{3+}, followed by a $q7$ jump, yielding an overall migration barrier of 2.16 eV. For jumps involving split interstitials, the jumping Ga atom is boldfaced and underlined in the defect notation.

2. Ga interstitial

For Ga_i we consider both the 3+ and 1+ charge states, in which Ga_{iac1} and Ga_{iad2} are the favored configurations, respectively. Figure 5 shows overall migration paths and barriers for different crystal directions. Note that, for split interstitials, the migration paths are drawn from the Ga site (as in Fig. 1), but either of the two Ga atoms sharing the site could make a jump (the other becoming substitutional). For jumps involving split interstitials in Fig. 5, the jumping Ga atom is therefore boldfaced and underlined in the defect notation below the plot.

We start with the overall migration paths and barriers for the 3+ charge state. An intuitive mechanism for Ga_{iac1}^{3+} migration along [010] would be for the Ga ion located near the ia site to move within the large eight-sided channel [47]. Such a mechanism yields a low overall migration barrier of 0.72 eV, as shown in Fig. 5(a). The interstitial makes a $q11$ jump from the Ga1 to the if site, resulting in the regular-interstitial configuration Ga_{if}. This is followed by a symmetrically

equivalent jump to form Ga_{iac1} at the next Ga1 site. Thus, the overall route consists of two consecutive $q11$ jumps.

For the [100] direction, we obtain a slightly higher barrier of 1.02 eV, as shown in Fig. 5(b). The limiting step is when Ga_{if} makes a $q13$ jump to form Ga_{iac1} on the other side of the large eight-sided channel. For this direction, the migration does not involve the same Ga ion along the entire route. Indeed, after crossing the eight-sided channel, the Ga_{iac1} split interstitial must cross the irregular-hexagon channel (equivalent to step one for migration along [001], as shown in Fig. 5(c) and described below). In this final step, the Ga_{if} that made the $q13$ jump across the eight-sided channel becomes Ga1 substitutional, and two different Ga ions form a Ga_{iac1} at the next Ga1 site. This must be considered when interpreting Ga migration in β-Ga_2O_3 using isotopes. After such an event, further migration of the tracer must occur through a self-diffusion mechanism mediated by V_{Ga} or Ga_i.

For migration along [001], shown in Fig. 5(c), we obtain an overall migration barrier of 0.80 eV. The Ga_{iac1} forms an equivalent Ga_{iac1} split interstitial on the other side of the irregular-hexagon channel by making two consecutive $q7$ jumps via the regular-interstitial configuration Ga_{ic}. This is followed by reorientation of Ga_{iac1} into a Ga_{iab1} split interstitial on the same Ga1 site (the Ga ion located near the ic site uses the $q16$ path to reach the ib site). Ga_{iab1} then similarly crosses the irregular-hexagon channel through two consecutive $q9$ jumps via the Ga_{ib} configuration, followed by reorientation from Ga_{iab1} to Ga_{iac1}. The overall route is thus $q7 \rightarrow q7 \rightarrow q16 \rightarrow q9 \rightarrow q9 \rightarrow q16$. An alternative way to view this mechanism is that the Ga ion located within the irregular-hexagon channel migrates along the [001] direction using the $q16$ path, displacing Ga1 ions into ia sites to form Ga_{iac1} and Ga_{iab1} along the way.

Migration of Ga_i^+ along [010] proceeds through a pathway similar to the one found for the 3+ charge state. After transformation of Ga_{iad2} into Ga_{iac1} though the $q4q5$ path, the interstitial can migrate along [010] by making consecutive $q11$ jumps via the if site. The resulting overall migration barrier is 0.92 eV, which is only slightly higher than the 0.72 eV obtained for Ga_i^{3+}.

For all migration paths of Ga_i^+ occurring within the large eight-sided channel, we find that the jumping Ga ion remains in a dimer with at least one other Ga ion along the entire route, i.e., a spatially localized KS defect state is found in the band gap for every image in the NEB calculation. However, this is not the case for the $q7$ and $q9$ paths, which cross the irregular-hexagon channels. This is because no Ga-Ga dimer could be stabilized for Ga_{ib} and Ga_{ic}. This result indicates that the $q7$ and $q9$ jumps can take place more easily if Ga_i^+ is first ionized into Ga_i^{3+} [49]. The migration barriers for these paths are thus estimated as the sum of the energy cost of the two processes: (i) thermal emission of two electrons from Ga_i^+ to the CBM, and (ii) passage over a lower migration barrier as Ga_i^{3+}. For the $q7$ path, the energy cost to thermally ionize Ga_{iac1}^+ into Ga_{iac1}^{3+} plus two electrons at the CBM is 1.06 eV, and the migration barrier of Ga_{iac1}^{3+} is 0.74 eV, resulting in a total barrier of 1.80 eV. Similar analysis for $q9$ yields a Ga_{iab1}^+ ionization energy of 0.94 eV, a Ga_{iab1}^{3+} migration barrier of 0.55 eV and a total barrier of 1.49 eV.
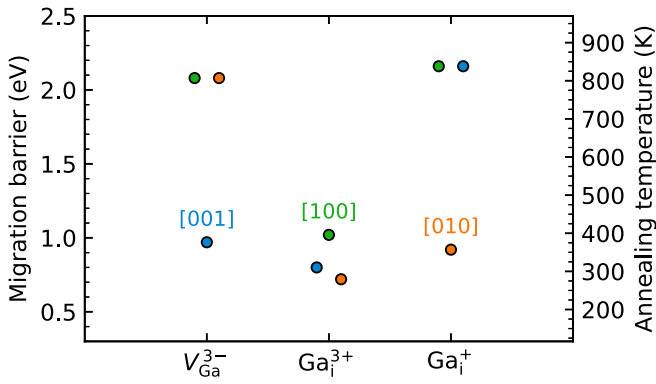
FIG. 6. Overall migration barriers for V_{Ga}^{3-}, Ga_i^{3+}, and Ga_i^+ along the [001] (blue), [010] (orange), and [100] (green) crystal directions. The right-hand side axis is the estimated defect annealing temperature $T_a = E_m \times 388$ K/eV (see text).

As mentioned, Ga_i^+ can transform relatively easily between different configurations occurring within the large eight-sided channel [those displaying a deep $(3 + /+)$ level in Fig. 3]. However, diffusion along the [001] and [100] directions require Ga_i^+ to cross between different eight-sided channels. For both the [001] and [100] directions, we find that the rate-limiting step is the thermal ionization of Ga_{iac1}^+ followed by a $q7$ jump into the irregular-hexagon channel (1.80 eV total barrier, as described above). Accounting for the 0.36 eV difference between Ga_{iac1}^+ and the global-minimum Ga_{iad2}^+ configuration, the overall migration barrier becomes 2.16 eV.

Since diffusion of Ga_i^+ along [100] and [001] involves thermal emission and capture of electrons, we note that the diffusivity can be influenced by the recombination kinetics of the defect, which will also depend on the Fermi energy. The configurations in which charge emission and capture occur must be stable for a sufficiently long time. The diffusivity of Ga_i^+ can also be influenced by other possible ionization events, such as photoionization of Ga_i^+ and relaxation from Ga_i^{2+} to Ga_i^{3+}.

C. Comparison with experimental data

For comparison with experimental data, it can be useful to estimate the defect annealing temperature. Using harmonic transition state theory [50], the rate of the migration process is given by $\nu = \nu_0 \exp(-E_m/k_B T)$, where E_m is the migration barrier, k_B is the Boltzmann constant, and ν_0 is the attempt frequency, which we approximate by a typical phonon frequency of 10^{13} Hz. Assuming that migration will be observable when the transition rate reaches one jump per second, the annealing temperature will be given by $T_a = E_m \times 388$ K/eV [51]. The calculated migration barriers and defect annealing temperatures of V_{Ga} and Ga_i are visualized in Fig. 6.

The estimated annealing temperature for V_{Ga}^{3-} is about 375 K for the [001] direction, and 805 K for the remaining directions. The diffusivity of V_{Ga}^{3-} is thus far greater than previously predicted [14,15], and strongly anisotropic. For Ga_i, the lowest overall migration barriers in the 1+ and 3+ charge states translate into corresponding annealing temperatures of 355 and 270 K.

We note that migration barriers of triply charged defects such as V_{Ga}^{3-} and Ga_i^{3+} can be strongly affected by the presence of electric fields [52]. The migration-barrier lowering for a charged defect in an electric field can be estimated as $\Delta E_m = Eqd$, where E is the electric field strength along the direction of atomic migration, and d is the distance between the initial and transition state. The migration barriers of V_{Ga}^{3-} and Ga_i^{3+} could thus decrease by ∼0.5 eV for typical jump lengths and electric fields accessible in β-Ga_2O_3 (3 Å and 6 MV/cm).

We finally discuss our theoretical predictions in light of experimental data on irradiated material reported by Azarov *et al.* [53], Ingebrigtsen *et al.* [15], and Zimmermann *et al.* [16], where various effects of intrinsic defect migration were studied in the temperature range from 120 to 650 K. Azarov *et al.* [53] studied the radiation disorder buildup in the Ga sublattice of β-Ga_2O_3 crystals implanted with Ni, and observed the so-called dose-rate effect. An activation energy of 0.8 ± 0.1 eV was extracted in the temperature interval of 25–250 °C, and was attributed to V_{Ga} based on comparison with first-principles calculations [14,34,54]. Assuming a Fermi-level position where 3− is the stable charge state of V_{Ga}, such a low migration barrier can only be explained by the three-split mechanism, which enables V_{Ga} diffusion along [001] with a 0.97 eV overall barrier. The minimum overall migration barriers of 0.92 and 0.70 eV for Ga_i^+ and Ga_i^{3+}, respectively, also suggest Ga_i as a likely candidate for the extracted activation energy.

Ingebrigtsen *et al.* [15] studied the thermally activated recovery of charge carriers in proton irradiated β-Ga_2O_3, which was observed upon heating in the temperature range from about 400 to 650 K. Based on formation energies calculated for primary intrinsic defects in different charge states, the compensation was attributed to Fermi level pinning by V_{Ga} and Ga_i (and possibly Ga_O) at least ∼0.5 eV below the CBM. Compensation by O_i acceptors was considered less likely, as O_i is extremely mobile with a theoretically predicted barrier of 0.12 eV for diffusion along [010] [15]. By modeling the charge carrier recovery as a defect reaction with second-order kinetics, an activation energy of ∼1.2 eV was obtained. There are several possible defect reactions that could contribute to the observed recovery, potentially also involving defect complexes and impurities, as discussed in detail by Ingebrigtsen *et al.* [15]. The present results suggest that V_{Ga} and Ga_i will be mobile during the heat treatment, with migration barriers close to the ∼1.2 eV activation energy, and their diffusion could contribute to the recovery.

Zimmermann *et al.* [16] performed steady-state photocapacitance (SSPC) measurements on β-Ga_2O_3 implanted with He at 120 K. A defect signature labeled T_3 was introduced with a linear dependence on the accumulated He fluence, but disappeared after exposing the sample to room temperature. Based on comparison with theoretical predictions, the signature was tentatively attributed to the photoionization of Ga_i^+ or a metastable configuration of V_{Ga}^{3-}, where the former candidate was envisioned to start diffusing at room temperature, and the latter to transform into the global-minimum configuration V_{Ga}^{ic} at room temperature. According to the present calculations, showing low migration barriers of 0.92 and 0.70 eV for Ga_i^+

and Ga_i^{3+}, such a scenario is indeed plausible. For V_{Ga}^{3-}, we calculate barriers of 0.34, 0.66, 0.66, and 0.69 eV for the V_{Ga1}, V_{Ga2}, V_{Ga}^{ia}, and V_{Ga}^{ib} configurations, respectively, to transform into V_{Ga}^{ic}. These barriers suggest that some of the transformations could be suppressed at 120 K. It should be noted, however, that photoionization could alter the transformation dynamics. As shown in Fig. 2, the relative formation energy of different V_{Ga} configurations depends on the charge state.

IV. CONCLUSION

In summary, we have used first-principles calculations and the NEB method to calculate energy barriers for the migration of V_{Ga} and Ga_i in β-Ga_2O_3. The migration barrier of V_{Ga}^{3-} is found to depend strongly on the crystal direction: 2.08 eV for the [100] and [010] directions, and 0.97 eV for the [001] direction. The low barrier found for the latter direction is enabled by a mechanism for transformation between different split-vacancy configurations [40], where the intermediate state consists of a three-split configuration rather than the energetically unfavorable V_{Ga1}^{3-}. This result further highlights the importance of split vacancies in β-Ga_2O_3 [14,31,32,35,39].

Ga_i^{3+} exhibits similar migration barriers of 0.72, 0.80, and 1.02 eV for the [010], [001], and [100] directions, respectively. The 1+ charge state is associated with the formation of a Ga-Ga dimer, resulting in a deep thermodynamic $(3 + /+)$ transition level located 0.4–0.9 eV below the conduction-band minimum. The Ga-Ga dimer can only be stabilized for Ga_i

configurations occurring within the large eight-sided channel, leading to preferential migration along [010] with a barrier of 0.92 eV. An overall barrier of 2.16 eV is found for the remaining directions, where the limiting step is found to involve thermal ionization of Ga_i^+ followed by a jump as Ga_i^{3+}.

[1] C. Janowitz, V. Scherer, M. Mohamed, A. Krapf, H. Dwelk, R. Manzke, Z. Galazka, R. Uecker, K. Irmscher, R. Fornari, M. Michling, D. Schmeißer, J. R. Weber, J. B. Varley, and C. G. Van de Walle, New J. Phys. **13**, 085014 (2011).

[2] F. Alema, Y. Zhang, A. Osinsky, N. Orishchin, N. Valente, A. Mauze, and J. S. Speck, APL Mater. **8**, 021110 (2020).

[3] E. G. Víllora, K. Shimamura, Y. Yoshikawa, K. Aoki, and N. Ichinose, J. Cryst. Growth **270**, 420 (2004).

[4] H. Aida, K. Nishiguchi, H. Takeda, N. Aota, K. Sunakawa, and Y. Yaguchi, Jpn. J. Appl. Phys. **47**, 8506 (2008).

[5] A. Azarov, V. Venkatachalapathy, L. Vines, E. Monakhov, I.-H. Lee, and A. Kuznetsov, Appl. Phys. Lett. **119**, 182103 (2021).

[6] A. Mauze, Y. Zhang, T. Itoh, T. E. Mates, H. Peelaers, C. G. Van de Walle, and J. S. Speck, J. Appl. Phys. **130**, 235301 (2021).

[7] H. Peelaers, J. L. Lyons, J. B. Varley, and C. G. Van de Walle, APL Mater. **7**, 022519 (2019).

[8] M. Wang, S. Mu, and C. G. Van de Walle, in *Oxide-based Materials and Devices XIII*, edited by F. H. Teherani and D. J. Rogers (SPIE, Bellingham, WA, 2022).

[9] Y. K. Frodason, C. Zimmermann, E. F. Verhoeven, P. M. Weiser, L. Vines, and J. B. Varley, Phys. Rev. Mater. **5**, 025402 (2021).

[10] M. E. Ingebrigtsen, A. Y. Kuznetsov, B. G. Svensson, G. Alfieri, A. Mihaila, and L. Vines, J. Appl. Phys. **125**, 185706 (2019).

[11] C. Zimmermann, E. F. Verhoeven, Y. K. Frodason, P. M. Weiser, J. B. Varley, and L. Vines, J. Phys. D: Appl. Phys **53**, 464001 (2020).

[12] A. Y. Polyakov, I.-H. Lee, A. Miakonkikh, A. V. Chernykh, N. B. Smirnov, I. V. Shchemerov, A. I. Kochkova, A. A. Vasilev, and S. J. Pearton, J. Appl. Phys. **127**, 175702 (2020).

[13] V. M. Reinertsen, P. M. Weiser, Y. K. Frodason, M. E. Bathen, L. Vines, and K. M. Johansen, Appl. Phys. Lett. **117**, 232106 (2020).

[14] A. Kyrtsos, M. Matsubara, and E. Bellotti, Phys. Rev. B **95**, 245202 (2017).

[15] M. E. Ingebrigtsen, A. Y. Kuznetsov, B. G. Svensson, G. Alfieri, A. Mihaila, U. Badstübner, A. Perron, L. Vines, and J. B. Varley, APL Mater. **7**, 022510 (2019).

[16] C. Zimmermann, V. Rønning, Y. Kalmann Frodason, V. Bobal, L. Vines, and J. B. Varley, Phys. Rev. Mater. **4**, 074605 (2020).

[17] G. Henkelman, B. P. Uberuaga, and H. Jansson, J. Chem. Phys. **113**, 9901 (2000).

[18] P. E. Blöchl, Phys. Rev. B **50**, 17953 (1994).

[19] G. Kresse and D. Joubert, Phys. Rev. B **59**, 1758 (1999).

[20] G. Kresse and J. Furthmüller, Phys. Rev. B **54**, 11169 (1996).

[21] J. Heyd, G. E. Scuseria, and M. Ernzerhof, J. Chem. Phys. **118**, 8207 (2003).

[22] J. Heyd, G. E. Scuseria, and M. Ernzerhof, J. Chem. Phys. **124**, 219906 (2006).

[23] A. V. Krukau, O. A. Vydrov, A. F. Izmaylov, and G. E. Scuseria, J. Chem. Phys. **125**, 224106 (2006).

[24] J. Åhman, G. Svensson, and J. Albertsson, Acta Crystallogr. **C52**, 1336 (1996).

[25] A. Baldereschi, Phys. Rev. B **7**, 5212 (1973).

[26] C. Freysoldt, B. Grabowski, T. Hickel, J. Neugebauer, G. Kresse, A. Janotti, and C. G. Van de Walle, Rev. Mod. Phys. **86**, 253 (2014).

[27] C. Freysoldt, J. Neugebauer, and C. G. Van de Walle, Phys. Rev. Lett. **102**, 016402 (2009).

[28] Y. Kumagai and F. Oba, Phys. Rev. B **89**, 195205 (2014).

[29] J. Sun, A. Ruzsinszky, and J. P. Perdew, Phys. Rev. Lett. **115**, 036402 (2015).

[30] M. E. Bathen, J. Coutinho, H. M. Ayedh, J. Ul Hassan, I. Farkas, S. Öberg, Y. K. Frodason, B. G. Svensson, and L. Vines, Phys. Rev. B **100**, 014103 (2019).

[31] J. B. Varley, H. Peelaers, A. Janotti, and C. G. Van de Walle, J. Phys.: Condens. Matter **23**, 334212 (2011).

[32] J. M. Johnson, Z. Chen, J. B. Varley, C. M. Jackson, E. Farzana, Z. Zhang, A. R. Arehart, H.-L. Huang, A. Genc, S. A. Ringel, C. G. Van de Walle, D. A. Muller, and J. Hwang, Phys. Rev. X **9**, 041027 (2019).

[33] K. Momma and F. Izumi, J. Appl. Crystallogr. **44**, 1272 (2011).

[34] M. E. Ingebrigtsen, J. B. Varley, A. Y. Kuznetsov, B. G. Svensson, G. Alfieri, A. Mihaila, U. Badstöbner, and L. Vines, Appl. Phys. Lett. **112**, 042104 (2018).

[35] P. Weiser, M. Stavola, W. B. Fowler, Y. Qin, and S. Pearton, Appl. Phys. Lett. **112**, 232104 (2018).

[36] Y. Qin, M. Stavola, W. B. Fowler, P. Weiser, and S. J. Pearton, ECS J. Solid State Sci. Technol. **8**, Q3103 (2019).

[37] H. J. von Bardeleben, S. Zhou, U. Gerstmann, D. Skachkov, W. R. L. Lambrecht, Q. D. Ho, and P. Deák, APL Mater. **7**, 022521 (2019).

[38] D. Skachkov, W. R. L. Lambrecht, H. J. von Bardeleben, U. Gerstmann, Q. D. Ho, and P. Deák, J. Appl. Phys. **125**, 185701 (2019).

[39] A. Karjalainen, V. Prozheeva, K. Simula, I. Makkonen, V. Callewaert, J. B. Varley, and F. Tuomisto, Phys. Rev. B **102**, 195207 (2020).

[40] W. B. Fowler, M. Stavola, Y. Qin, and P. Weiser, Appl. Phys. Lett. **117**, 142101 (2020).

[41] P. Deák, Q. Duy Ho, F. Seemann, B. Aradi, M. Lorke, and T. Frauenheim, Phys. Rev. B **95**, 075208 (2017).

[42] B. E. Kananen, L. E. Halliburton, K. T. Stevens, G. K. Foundos, and N. C. Giles, Appl. Phys. Lett. **110**, 202104 (2017).

[43] J. B. Varley, A. Janotti, C. Franchini, and C. G. Van de Walle, Phys. Rev. B **85**, 081109(R) (2012).

[44] Y. K. Frodason, K. M. Johansen, L. Vines, and J. B. Varley, J. Appl. Phys. **127**, 075701 (2020).

[45] T. Zacherle, P. C. Schmidt, and M. Martin, Phys. Rev. B **87**, 235206 (2013).

[46] S. Lany and A. Zunger, Phys. Rev. Lett. **93**, 156404 (2004).

[47] C. Zimmermann, Y. K. Frodason, A. W. Barnard, J. B. Varley, K. Irmscher, Z. Galazka, A. Karjalainen, W. E. Meyer, F. D. Auret, and L. Vines, Appl. Phys. Lett. **116**, 072101 (2020).

[48] See Supplemental Material at http://link.aps.org/supplemental/10.1103/PhysRevB.107.024109 for videos showing the migration pathways for each crystal direction.

[49] J. C. Bourgoin, J. W. Corbett, and H. L. Frisch, J. Chem. Phys. **59**, 4042 (1973).

[50] G. H. Vineyard, J. Phys. Chem. Solids **3**, 121 (1957).

[51] D. Steiauf, J. L. Lyons, A. Janotti, and C. G. Van de Walle, APL Mater. **2**, 096101 (2014).

[52] K. H. Warnick, Y. Puzyrev, T. Roy, D. M. Fleetwood, R. D. Schrimpf, and S. T. Pantelides, Phys. Rev. B **84**, 214109 (2011).

[53] A. Azarov, V. Venkatachalapathy, E. V. Monakhov, and A. Y. Kuznetsov, Appl. Phys. Lett. **118**, 232101 (2021).

[54] M. A. Blanco, M. B. Sahariah, H. Jiang, A. Costales, and R. Pandey, Phys. Rev. B **72**, 184103 (2005).